

Laser Entrance Window Transmission and Reflection Measurements for Preheating in Magnetized Liner Inertial Fusion

Introduction

Magnetized liner inertial fusion (MagLIF)^{1,2} relies on the compression of a cylindrical, axially magnetized, preheated plasma to achieve the temperature and radially integrated magnetic field (BR) necessary for fusion ignition: ~ 7 keV and $0.6 \text{ T}\cdot\text{m}$ for DT (deuterium–tritium) fusion, respectively.³ The Z machine has achieved neutron-averaged ion temperatures of up to 3 keV and BR of up to $0.4 \text{ T}\cdot\text{m}$ by compressing deuterium-filled beryllium liners, with an initial 10-T axial magnetic field, preheated with 2.5 kJ of 527-nm light from the Z-Beamlet laser.⁴

Laser-driven MagLIF is now being developed on the OMEGA laser^{5–7} to study scaling by driving a target $\sim 10\times$ smaller in linear dimensions than those used on Z, dictated by the $\sim 1000\times$ lower drive energy (from ~ 10 MJ on Z to ~ 10 kJ on OMEGA). OMEGA also provides a higher shot rate, better diagnostic access, and x-ray and neutron diagnostics with a greater dynamic range than can be achieved on Z, facilitating parameter scans. Figure 154.36 illustrates MagLIF on Z and OMEGA and the scaling between them.

The initial point design for laser-driven MagLIF on OMEGA is described by Davies *et al.*,⁶ a brief overview of the design

work and initial experiments is given by Barnak *et al.*,⁵ and a more-detailed description of compression-only experiments and simulations is given by Hansen *et al.*⁷ Here we describe some of the results from our very first experiment, carried out during the initial design phase, looking at just the laser preheating. MagLIF targets require a preheat laser entrance window that can hold the gas in the target, yet allow sufficient laser energy to enter the gas. A similar situation is also encountered with gas-filled hohlraums, although the gas pressures used are lower, allowing a thinner window to be used. We measured the laser transmission of polyimide foils, selected for our window material, with a calorimeter and three time-resolved spectrometers, at different angles; we also measured the reflection from foils only and from full targets with the time-resolved spectrometers. These measurements were intended to show if sufficient laser energy could be coupled into the target to achieve the goal of preheating to a mean temperature ≥ 100 eV, established by the point-design simulations.⁶ Of particular concern was the possibility of significant backscatter caused by parametric instabilities in the expanding foil plasma. Transmission and reflection measurements can also be directly compared to results from hydrodynamic simulations with ray tracing, providing a test of our simulation capabilities. We used the 2-D code *DRACO*⁸ to simulate the experiments.

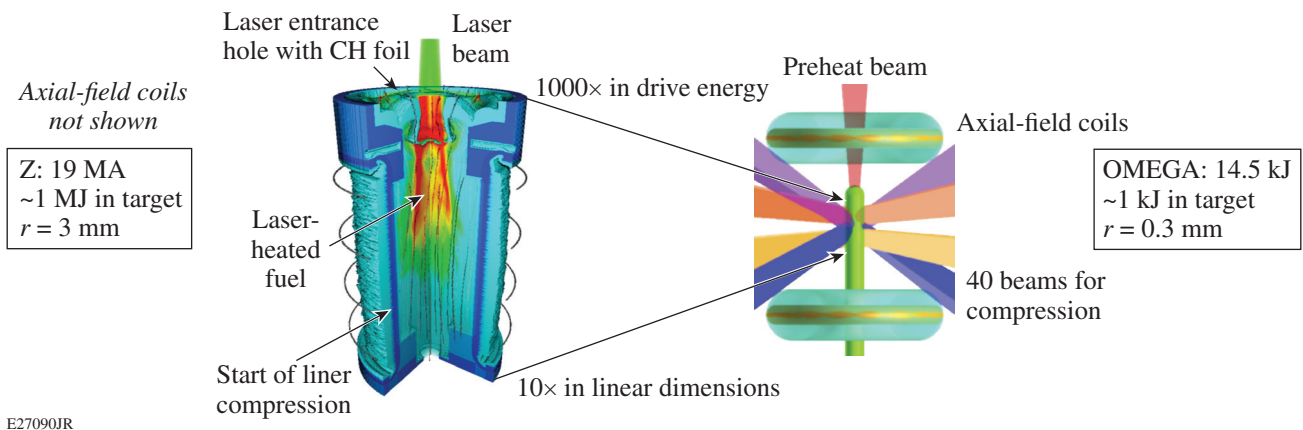


Figure 154.36 An illustration of MagLIF on Z and OMEGA, roughly to scale. The image for Z is from a 3-D simulation and the image for OMEGA is from a 3-D design drawing.

Preheating experiments for Z-scale MagLIF targets have been carried out using the Z-Beamlet laser,⁹ OMEGA EP,¹⁰ and OMEGA; for potential ignition-scale MagLIF targets, experiments were carried out on the NIF (National Ignition Facility). The targets in these experiments were all significantly larger than used here and the laser energies and powers were higher, but there is some overlap with the laser intensities and foil thickness used here.

The following sections describe the experimental and simulation methods, respectively; present and analyze the results from both the experiments and simulations; and present the conclusions.

Experimental Methods

1. Targets

The point-design process led to the choice of a 0.6-mm-outer-diam plastic (CH) target, based on available phase plates, with a $\leq 30\text{-}\mu\text{m}$ -thick shell and a deuterium fuel density from 1.5 to 2.7 mg/cm^3 , corresponding to a pressure of 9 to 16 atm at room temperature, based on simulated neutron yields and fuel convergence ratios.⁶

Polyimide ($\text{C}_{15}\text{H}_5\text{N}_3\text{O}_2$, 1.44 g/cm^3) was chosen for the window material because of its high ultimate tensile strength and low mean atomic number. The window foils were glued to a plastic washer using compliant glue, and the washers were glued to the outside of the cylindrical targets using epoxy, with the foil on the front of the target. Foils mounted on washers with a 1.1-mm inner diameter were used to measure laser

transmission. In a preliminary test, a 2- μm -thick foil burst at a pressure of about 18 atm, so this thickness was chosen for subsequent experiments. The polyimide film delivered by Schafer for these experiments was measured to have a thickness of $1.84 \pm 0.01\ \mu\text{m}$. Z experiments, and associated experiments studying just the preheating, have used 0.5- to 3- μm -thick polyimide as the laser entrance window. During experiments, a series of targets failed at 14 atm, with the washer–target joint being the principle issue, so the experiments described here were carried out with an initial fill pressure of 11 atm. Slow leaks led to the pressure at shot time, measured using a pressure transducer on the fill tube at the back of the target, being lower than 11 atm; final pressures varied from 5.2 to 10.9 atm. Design drawings of the targets are shown in Fig. 154.37.

The cylindrical targets for these experiments were made of 30- μm -thick fluorinated parylene-AF4 ($\text{C}_8\text{H}_4\text{F}_4$, 1.32 g/cm^3 , also denoted by the suffixes SF, HT, and VT), and the deuterium gas was doped with 2% Ne, by atom, for x-ray diagnostics.

The foils on the full targets bowed outward under the pressure, as can be seen in Fig. 154.38(b), which is the only image of a full target where the foil is visible because the metal x-ray shield was not attached. The force on the foils certainly exceeded the yield stress; flat-plate calculations showed that they would rupture below 10 atm, but for a hemisphere, the stress is below the ultimate tensile strength. Foil bowing can also be caused by motion of the glue joint, which was chosen to be compliant to reduce the risk of tearing, so we cannot be certain of the actual thickness of the foils on the full targets.

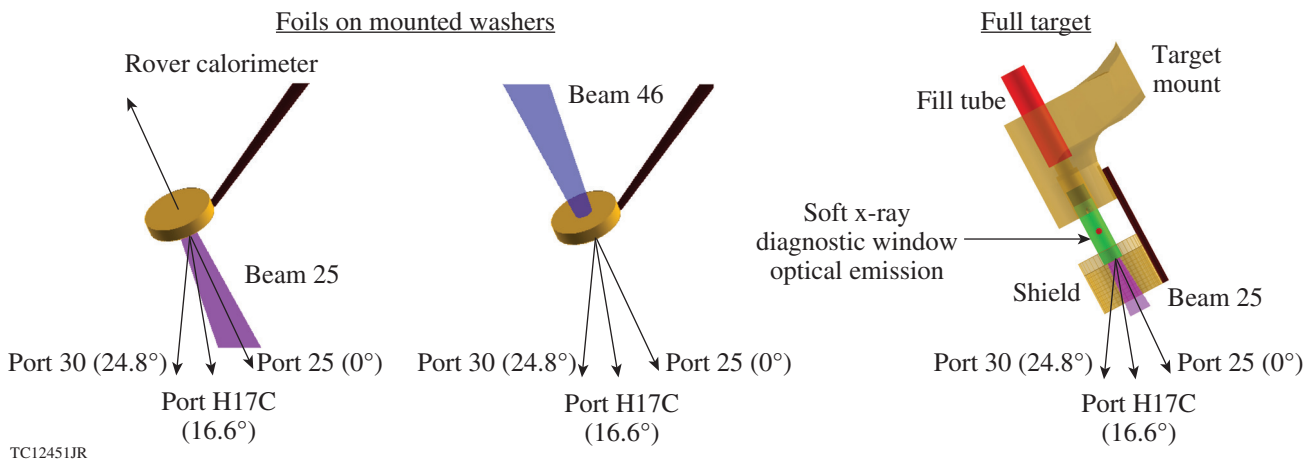
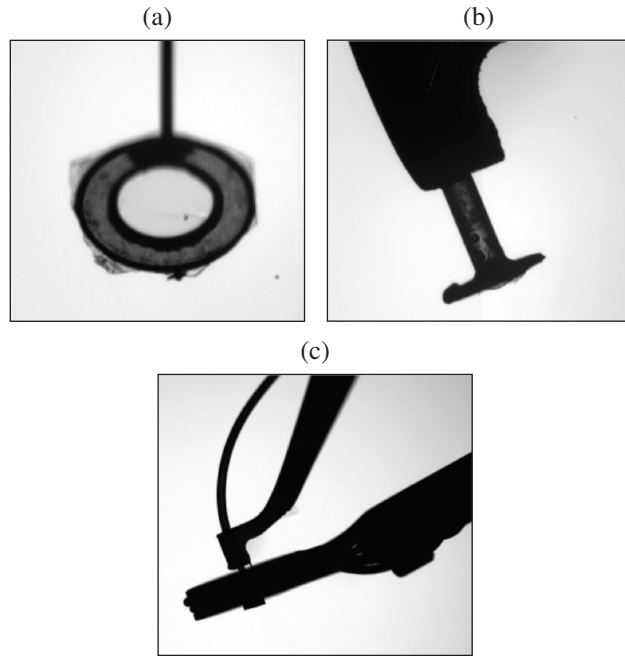


Figure 154.37

Design drawings of the targets used in the experiments, indicating the beams used and the ports through which light was collected. The full targets had a polyimide window on the side and a metal shield around the entrance window for the sake of the soft x-ray diagnostics (not considered here).



TC12450JR

Figure 154.38

Images from the OMEGA Target Viewing System: (a) a foil target from shot 76671, (b) a full target from shot 76683, which was the only one that had no cylindrical metal shield around the entrance window, and (c) a full target with a magnetic-field coil from shot 76673, with a lower magnification than (a) and (b).

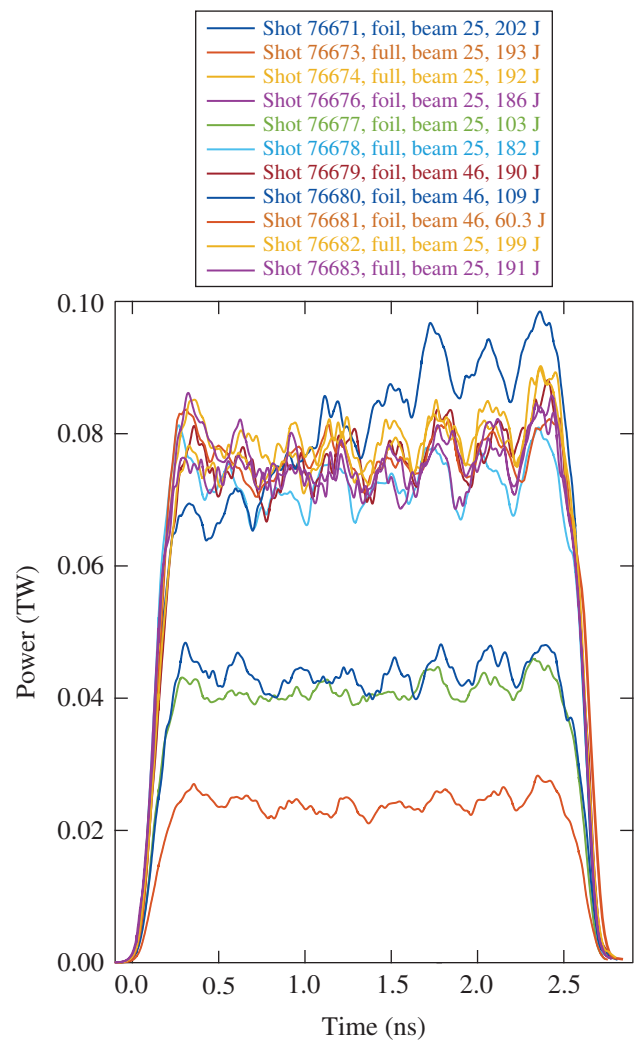
MagLIF targets require an axial magnetic field, ideally around 30 T (Refs. 1 and 6). Therefore, a magnetic field was applied on two full target shots using a single multiple-turn coil near the center, which can be seen in Fig. 154.38(c). The radius of the coil was sufficient to give a roughly constant field of 15 T over the region of interest.

2. Laser Parameters

The pulse shape for the preheat beam must be the same as the pulse shape for the compression beams because OMEGA has independent pulse shaping on only one of the three legs of beams, and beams from all three legs are necessary for the compression; therefore, a square-shaped pulse was used.⁶ Preliminary 1-D simulations indicated that a 2.5-ns pulse was ideal for the compression; therefore, we used this pulse duration. These simulations did not take into account, however, the rapid fall in energy on target above 1 ns, resulting from the fall in frequency-conversion efficiency with power. When the measured maximum energies were used in the simulations,⁶ the ideal pulse duration was found to be 1.5 ns. The longer pulse used in these experiments is not a significant factor because it still provides the information we need for a 1.5-ns pulse of the same power since we have time-resolved diagnostics.

MagLIF on Z uses a prepulse to explode the window, which minimizes the energy absorbed by the window and the density of the window plasma seen by the main pulse. On the other hand, it gives the window plasma more time to propagate into the target.

Figure 154.39 shows the measured pulse shapes for all of the shots taken. The laser power on target takes into account initial laser energy, frequency-conversion efficiency, and the transmission of the phase plate and blast window assembly. The measurements should be accurate to better than $\pm 5\%$. With the exception of the first shot, where the power increases near the end, the pulse shapes are very similar, so the only significant variation between shots is the total energy, as intended.



E27091JR

Figure 154.39

Measured pulse shapes for all of the shots taken, indicating the target type, beam number, and total energy on target.

Smoothing by spectral dispersion (SSD), a distributed polarization rotator (DPR), and a distributed phase plate (DPP) were used to give the best-possible laser uniformity available on OMEGA. The smallest phase plate available on OMEGA that gives an almost round, smooth laser spot was used; a smaller phase plate exists but it gives an almost square spot with considerable intensity modulations. An equivalent-target-plane image of the chosen phase plate is shown in Fig. 154.40, including a DPR and SSD, taken after the initial design work and experiments were completed. A Gaussian

$$I = I_0 \exp\left(-\frac{r^2}{R^2}\right) \quad (1)$$

was found to give an adequate fit, with $R = 108.8 \pm 0.1 \mu\text{m}$ (95% confidence bounds), using a 2-D fitting routine, which is shown in Fig. 154.40. The peak intensity for a total energy E J in 2.5 ns is

$$I_0 = 1.08 \times 10^{12} E \text{ W/cm}^2. \quad (2)$$

A super-Gaussian fit to an older image (original data no longer available) gave

$$I = 7.60 \times 10^{11} E \exp\left\{-\left[\left(\frac{r}{126.8 \mu\text{m}}\right)^2\right]^{1.195}\right\} \text{ W/cm}^2, \quad (3)$$

which was used to simulate the initial preheat.⁶

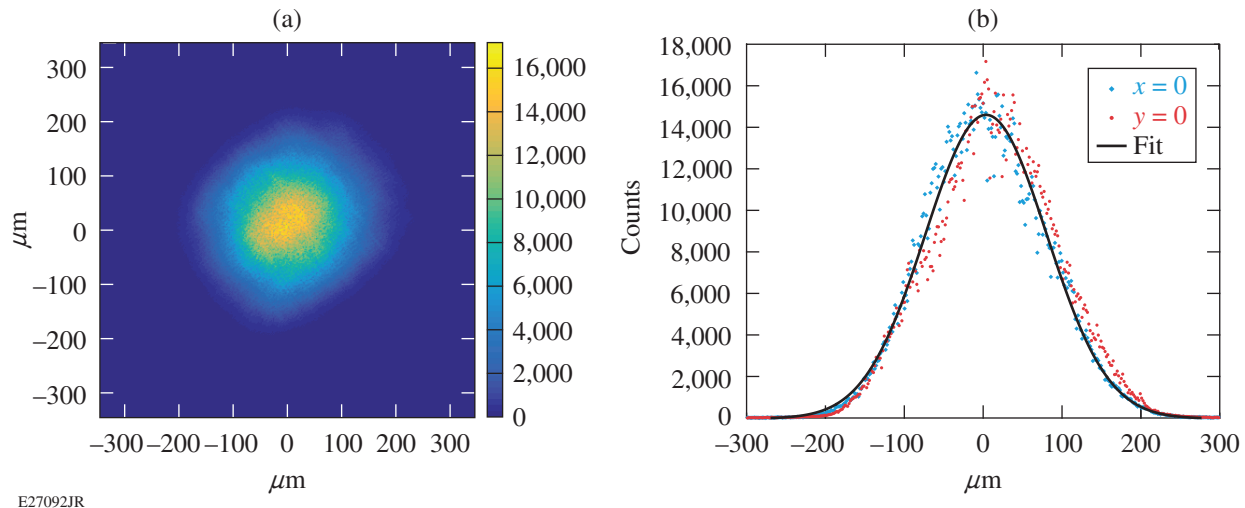


Figure 154.40

(a) Equivalent-target-plane image obtained with the distributed phase plate used in the experiments, including a distributed polarization rotator, and with smoothing by spectral dispersion on; (b) horizontal and vertical lineouts through the center of the image with the Gaussian fit.

Preliminary 2-D simulations for a deuterium fill pressure of 10 atm indicated that a total energy of 200 J in 2.5 ns would be sufficient to achieve a mean temperature of 200 eV over a 1-mm-long region of the gas ahead of the window plasma, which was the preheat temperature chosen for the point design. A preheat scan in the 1-D simulations for the point design⁶ showed a threshold preheat of 100 eV, for which 2-D simulations indicated a total energy of 60 J in 2.5 ns would be sufficient. As an intermediate value, we chose 100 J, so the requested energies on target were 200, 100, and 60 J, corresponding to mean laser powers of 80, 40, and 24 GW, and time-averaged peak intensities of 2.2, 1.1, and $0.65 \times 10^{14} \text{ W/cm}^2$ [from Eq. (2)]. The actual on-target energies are reported in Fig. 154.39. Z experiments, and associated experiments studying only the preheating, have used laser powers from 0.2 to 1 TW and intensities from 0.5 to $5 \times 10^{14} \text{ W/cm}^2$.

3. Diagnostics

The diagnostics considered here are laser calorimeters and time-resolved spectra. OMEGA has two full-aperture backscatter stations (FABS) on Beamlines 25 and 30 that are at 24.6° to one another. These systems collect light coming back through the laser lens and separate it into two wavelength bands: one that includes 351 nm (the laser wavelength), intended for stimulated Brillouin scatter (SBS); and one at longer wavelengths, intended for stimulated Raman scatter (SRS) and two-plasmon decay (TPD), each of which is split between a calorimeter and a streaked spectrometer. The laser lenses are 30 cm in diameter and 180 cm from the target chamber center, so ports 25 and 30 cover $\pm 4.77^\circ$. A similar system is also implemented on two

smaller diagnostic ports; of interest here is port H17C that uses a 2.2225-cm-diam lens and is situated at 16.6° to Beamline 25, so it covers $\pm 0.35^\circ$. A calorimeter, known as the Rover, can be used to collect the light coming through any one of OMEGA's beam ports.

We used Beamline 25 on foil and full targets to measure time-resolved backscatter at $\theta = 0^\circ$, 16.6° , and 24.6° ; for the foil targets, we used the Rover calorimeter on opposing port 46 to measure total transmission along the original beam path. We then used Beamline 46 on foil targets to measure time-resolved transmission at $\theta = 0^\circ$, 16.6° , and 24.6° , using the measurement of the total transmitted energy to determine the filtering that would be required to avoid damaging the system. The diagnostic setup is illustrated in Fig. 154.37.

All of the measurements taken using the FABS and H17C are traditionally referred to as backscatter. Here we will refer to the measurements taken using Beamline 46 as transmission and the measurements taken using Beamline 25 as reflection. We will refer to the transmission and reflection measurements taken using 25 as direct since this corresponds to energy within the original beam cone, and to the transmission and reflection measurements taken using H17C and 30 as sidescatter since they correspond to energy outside the original beam cone.

For all except the direct transmission measurements, the signals on the calorimeters were too low to give the total energy, but the streaked spectrometers are more sensitive and did have a usable signal. To determine the total energies, the ratio between the energy registered by the calorimeters and the total signal on the streaked spectrometers was taken from four spherical implosion shots from the immediately preceding shot day, taking into account the differences in filtering. The standard errors from these energy calibrations are $\pm 7\%$ for 25, $\pm 16\%$ for H17C, and $\pm 14\%$ for 30; we assume that this is the dominant source of error. The uncertainty in the calibration of the Rover calorimeter is estimated to be $\pm 5\%$.

Some uncertainty exists in the relative timings of the signals in 25, H17C, 30, and the laser pulse. The OMEGA timing fiducial should be accurate to within ± 10 ps, but the sampling interval of the time-resolved spectrometers is ~ 15 ps, so the relative timing cannot be more accurate than this. It is possible that there is a greater systematic error in the determination of the relative values of $t = 0$ in the diagnostics.

Two soft x-ray imaging systems, a time-resolved soft x-ray spectrometer, and streaked optical pyrometry of the outer

surface of the cylinders were also fielded but will not be considered here.

Simulation Methods

The shots were simulated using the Eulerian version of the 2-D radiation–hydrodynamic code *DRACO*, which uses 3-D ray tracing with inverse bremsstrahlung energy deposition,⁸ which is the standard for these types of simulations.

Several simplifications were made to the targets: The foil was taken to be $1.8 \mu\text{m}$ thick rather than the measured value of $1.84 \mu\text{m}$. The glue was not considered. For the foil shots, the washer was not considered since its inner diameter was significantly greater than the laser spot. For the full targets, the washer was considered to be part of the cylinder, the curvature and possible stretching of the foil were not considered, and the cylinders were truncated after ~ 1.8 mm at an open boundary. Foil curvature is difficult to simulate on a rectangular Eulerian grid, and the exact shape is not known. The code cannot deal with vacuum, so, instead, hydrogen with a density of $1 \mu\text{g}/\text{cm}^3$ was used. The “vacuum” density was increased by a factor of 10 and found not to affect the results.

The 15-T axial magnetic field, applied on full-target shots 76673 and 76674, was not considered and is expected to have a negligible effect on the laser–foil interaction since the Hall parameter remains less than 1 and the magnetic pressure is negligible.

An axial grid spacing of $0.2 \mu\text{m}$ was used in the foil and was increased by 10% for each cell moving away from the foil. For the full targets, the axial grid spacing inside the cylinder was capped at $2.5 \mu\text{m}$. The radial grid spacing was $2.5 \mu\text{m}$ up to the edge of the cylinder and was increased by 10% per cell beyond. To test that the grid spacing was adequate, the axial grid spacing around the foil was reduced to $0.1 \mu\text{m}$, the radial grid spacing was reduced to $1 \mu\text{m}$, and the regions of uniform grid spacing were extended; it was found that these changes did not modify the results.

Defining $z = 0$ to be the center of the foil and the laser to enter from the positive z direction, the simulation box for the foil runs extended from approximately $z = -1.51$ mm to $z = 1.66$ mm and for full target runs from approximately $z = -1.82$ mm to $z = 4.3$ mm. Defining $r = 0$ to be the axis of rotational symmetry, the simulation box for the foil runs extended up to approximately $r = 0.581$ mm and for full target runs up to $r = 0.51$ mm. The boundary conditions were reflective at $r = 0$ and open for all other boundaries.

SESAME equations of state were used: for polyimide a table for mylar ($C_{10}H_8O_4$) was chosen, being the closest material available; for parylene-AF4, a table for polystyrene (CH) was chosen; and the neon-doped deuterium was treated as deuterium. To test the sensitivity to the equation of state, the polystyrene equation of state was also used for the polyimide and found to have no noticeable effect. Twelve-group radiation transport was used with opacities, emissivities, and mean ionization levels calculated by the *PrismSPECT* collisional-radiative-equilibrium model for the materials used. For the hydrogen “vacuum,” the ideal gas equation of state was applied and treated as fully ionized.

The standard Spitzer–Härm thermal conduction model was used with a flux limiter of 0.06. For one run (shot 76676), no flux limiter was also considered, which marginally increased the laser energy absorbed by the foil, increasing the difference between simulation and measurement.

The measured laser powers shown in Fig. 154.39 and the laser intensity profile given by Eq. (3) were used in the ray tracing. In one run (shot 76676), Eq. (1) was also used for the intensity profile. The 42% increase in peak intensity led to an upturn in transmission, explained in the next section, occurring about 0.05 ns earlier, and to a 2.35% increase in directly transmitted energy. The uncertainty in the actual laser parameters can be treated as an uncertainty in the simulation results, which is clearly less than the uncertainty in the measurements with which they are being compared. The simulations were started at -0.1 ns because there is laser power before the facility-defined $t = 0$, and a signal was detected in the time-resolved spectrometers before $t = 0$. Laser imprinting, which calculates the random intensity fluctuations expected for a beam with SSD, DPR, and DPP, was tested in some runs and found to make no noticeable difference in the results of interest. The boundary through which the rays enter and leave if reflected is set by the largest value of z for which electron density $n_e \geq 0.01 n_c$, where n_c is the critical density or the boundary of the simulation box, whichever is smaller. The ray-tracing routine simulates the FABS diagnostic by collecting rays at user-specified “ports,” assuming straight-line propagation outside the ray-tracing grid, and by calculating the frequency shift using the electron density and fluid velocity at the time step at which the ray tracing is carried out. When the actual diameter of the H17C port was used, no rays were collected, so it was increased by a factor of 10 and the energy was divided by a factor of 100 for comparison with the experimental results. In the code it is possible to make all six measurements simultaneously, so only foil shots 76676 (185.6 J), 76677 (102.6 J), and 76681 (60.3 J) were simulated

since these cover the full range of laser energies. For the full targets, only shots 76678 (181.8 J, 10.9 atm of fill pressure) and 76682 (198.6 J, 5.2 atm of fill pressure) were simulated since the energies on target were very similar for all full target shots and these represent the extremes in fill pressure. For comparison with the experimental results for other shots, the energies collected by the diagnostic ports in the code were scaled linearly with laser energy from the run with the closest energy. The results presented here used 1000 rays per radial cell. Runs with only 100 rays per cell gave very similar results but had too few rays in all but the direct transmission diagnostic.

Results

1. Foil Targets

The energies collected by the Rover calorimeter in port 46 and in the SBS (laser) channel of the time-resolved spectrometers in ports 25, H17C, and 30 are given in Table 154.IV with the simulated values underneath. No detectable signal was obtained in the SRS channel on any of our shots. No reflected energies were measured on the first shot because the initial filtering was too strong; the reflected energies turned out to be close to the detection threshold.

The most-significant results from Table 154.IV for the laser-driven MagLIF project are (1) direct transmission exceeds the simulated values by $\sim 10\%$ of the laser energy, so simulations would be expected to slightly underestimate gas heating; and (2) sidescatter of transmitted light is negligible, so direct laser heating of the wall should not be an issue. Sidescatter of transmitted light is a factor of roughly $100\times$ higher than simulated, but the simulations show that thermal conduction dominates wall heating;⁶ even increasing the laser energy incident on the wall by a factor of 100 would still make it a small contribution.

It is worth noting that thermal conduction into the wall during preheat is only an issue for the smaller targets used on OMEGA, not for those used on Z, because thermal diffusion time scales as r^2 , so it is not scale invariant. On Z, the shock generated by the preheating will reach the wall before thermal diffusion heats it to any significant extent. If there is sidescattered transmission on Z, it would dominate wall heating at early times, and the longer time scales on Z compared to OMEGA could lead to a significant direct laser contribution to wall blow-in.

To estimate the total sidescattered energies, we extrapolated from the energy per unit area in ports H17C and 30 using a Gaussian $\exp(-r^2/R^2)$ and a circular diffraction profile $J_1(r/R)/(r/R)$, where J is a Bessel function of the first kind, in $r \approx L\theta$, where L is the distance from target chamber center to

Table 154.IV: Results for foils, giving laser beam number, laser energy (E), and laser energy collected by the diagnostics in ports 46, 25, H17C, and 30, with simulated results underneath. The percentage in parentheses is with respect to the incoming energy per unit area at the laser port. Transmitted energies are shown in bold. The calibration errors are estimated at $\pm 5\%$ for the calorimeter used in 46, $\pm 7\%$ for 25, $\pm 16\%$ for H17C, and $\pm 14\%$ for 30, as explained in the text.

Beam	E (J)	46 (%) Simulation	25 (%) Simulation	H17C (%) Simulation	30 (%) Simulation
25	202	131 J (64) 113 J (56)	– –	– –	– –
25	186	116 J (62) 104 J (56)	85.3 mJ (0.046) 3.23 J (1.7)	0.161 mJ (0.016) 0.946 μ J (<0.001)	14.6 mJ (0.008) 27.3 μ J (<0.001)
25	103	60.3 J (59) 48.8 J (48)	51.2 mJ (0.050) 2.35 J (2.3)	0.101 mJ (0.018) 35.1 nJ (<0.001)	8.63 mJ (0.008) 1.55 μ J (<0.001)
46	190	– –	126 J (66) 106 J (56)	0.210 mJ (0.20) 13.3 μJ (0.01)	3.94 mJ (0.002) 0.319 mJ (<0.001)
46	109	– –	65.2 J (60) 51.8 J (48)	67.3 μJ (0.011) 13.8 μJ (0.002)	2.94 mJ (0.003) 0.306 mJ (<0.001)
46	60.3	– –	31.7 J (53) 23.6 J (39)	0.178 mJ (0.054) 7.56 μJ (0.002)	2.02 mJ (0.003) 0.196 mJ (<0.001)

the ports (1.8 m), to find the total energy outside port 25. These profiles were chosen because they represent, approximately, the initial laser profile and the profile of a plane wave passing through a circular hole, potentially a small hole initially made in the foil by the laser. The ratio of the energies per unit area in H17C and 30 determines R , and the magnitude of either signal determines the peak energy per unit area. We could not adequately fit the three measurements together with either a Gaussian or a variety of Bessel-based functions; any function with three free parameters could of course be used to extrapolate from the three measurements.

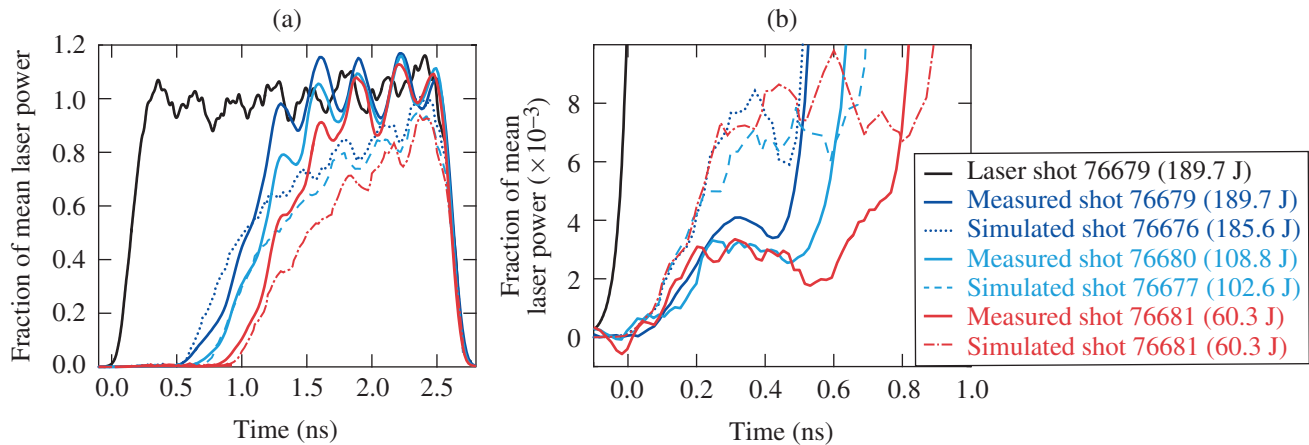
For transmission, the Gaussian extrapolation gave the fraction of sidescattered laser energy to be 0.82%, 0.33%, and 0.85%, and the circular diffraction extrapolation gave 0.72%, 0.82%, and 1.14%, for laser energies of 190, 109, and 60.3 J, respectively, which are not significant. The extrapolated energy in port 25 was always much less than the measured value. Circular diffraction gives a consistent trend with laser energy and less variation than the Gaussian, so it would appear to be a better assumption for sidescattered transmission.

For reflection, the circular diffraction extrapolation put too much energy into port 25 for two of the three foil shots. The Gaussian extrapolation put the *total* reflected energy at 0.6% of the laser energy for both of the foil shots that measured reflection, confirming that the total is negligible. According to this extrapolation, most of the energy is reflected outside of the incoming beam cone.

Using the equations for circular diffraction, or a Gaussian beam, it is possible to extrapolate back from the radius R at the detectors to a radius R_f at the foil of $L\lambda/2\pi R$, where L is distance from port to target (1.8 m) and λ is laser wavelength (351 nm). The circular diffraction extrapolation for transmission gave radii of 1.27, 1.25, and 0.77λ , for laser energies of 190, 109, and 60.3 J, respectively (the Gaussian extrapolation gave 0.84, 0.64, and 0.77λ). Treating the reflected signals in H17C and 30 as a Gaussian beam originating at the foil gave unphysically small values of R_f ; a diffuse reflection is probably a better description for these measurements.

The direct transmitted power as a function of time for the three laser energies used is shown in Fig. 154.41. The measurements show a rapid transition to total transmission, which occurs later for lower laser energies. The simulations adequately capture the initial increase in transmission, which occurs as the foil becomes underdense, as shown by the critical density contour in Fig. 154.42 at 0.45 ns, but the subsequent rise in transmission as the foil expands is slower and never quite reaches total transmission, which leads to an underestimate of the total transmitted energy.

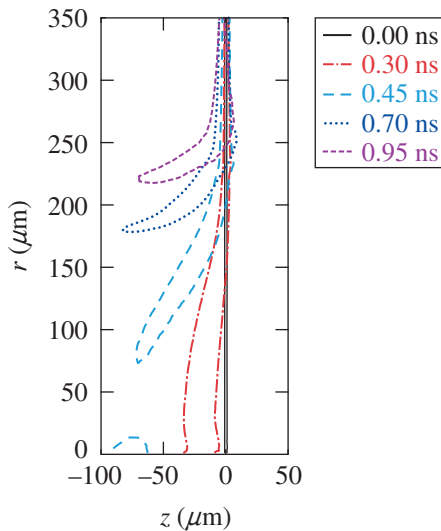
The falling edges of the direct transmission and laser pulse measurements shown in Fig. 154.41 match to within one point of the transmission measurements (~ 15 ps), indicating that the relative timings between 25 and the laser pulse are accurate. We do not have as clear a reference to determine the accuracy of the relative timings of H17C and 30. The agreement between



E27093JR

Figure 154.41

Direct transmitted laser power as a fraction of the mean laser power versus time for the three foil shots taken with Beamline 46, with the simulated results, and the laser power on target for one shot.



E27094JR

Figure 154.42

Critical-density contours at a sequence of times from the simulation of shot 76676 (foil, 186 J).

the direct transmitted laser power and the measured laser power indicates that the absolute energy calibration is accurate. The direct transmission does not show all of the structure seen in the laser pulse measurements because it has ~ 200 points versus ~ 1000 points for the laser pulse measurement.

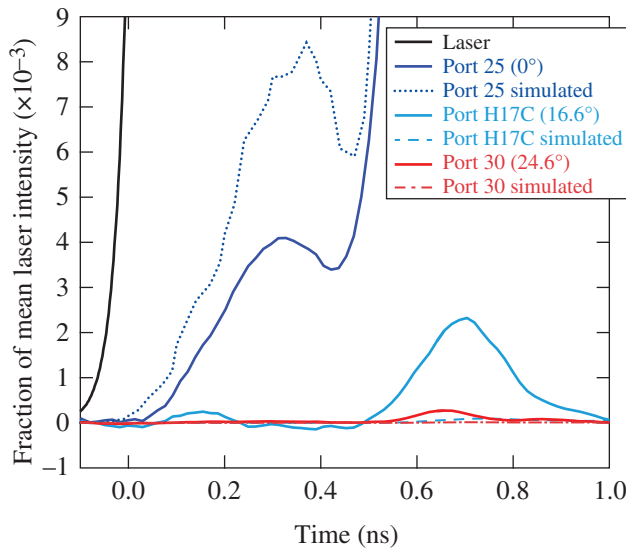
There is a small peak in direct transmitted power during the rising edge of the laser pulse, just before the sudden increase in transmission, which is captured in the simulations, although it is overestimated. The cold polyimide foil would transmit a

fraction of the laser light, and this fraction would fall as it is ionized by the laser. The instantaneous transmission cannot be accurately determined because of the noise in the measurements of both the laser power and the transmitted power and the uncertainty in their relative timings, which lead to large error bars, but it is clear from the rise in the laser power that transmission is falling during this phase. In the simulations, a minimum ionization level $Z = 0.11$ is imposed on the polyimide so it is initially at critical density to avoid high transmission and start inverse bremsstrahlung absorption. The optical depth of an overdense cell ($n_e \geq n_c$) is fixed at an arbitrary upper limit, which results in some transmission. The initial transmission in the simulation is therefore somewhat arbitrary. The transmission falls because the ionization level increases and the foil expands, increasing the width of the overdense region, as seen in Fig. 154.42, from 0 to 0.3 ns. Therefore, coincidentally, the simulations are comparable to the measurements on the rising edge of the pulse because the code has no accurate physical model for solids. Strictly speaking, the laser model is accurate for only ideal underdense ($n_e < n_c$) plasma. The agreement of the simulations with the measurements in this phase could be improved by modifying the minimum ionization level of polyimide and the optical depth of an overdense cell, but this would not be a physically meaningful agreement and might work only for the specific set of parameters considered.

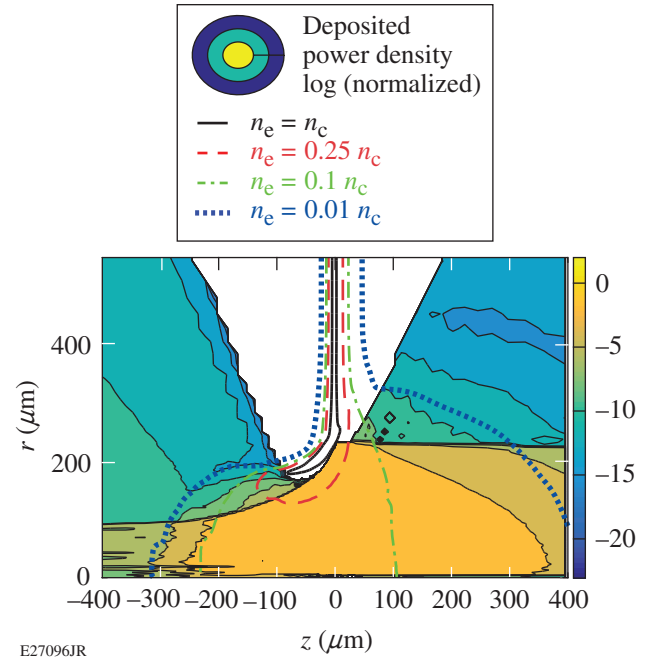
The final choice of pulse duration for laser-driven MagLIF was 1.5 ns, not the 2.5 ns used here, as discussed in the **Introduction** (p. 91). The time-resolved measurements show that the direct transmitted energy at 1.5 ns was 36.1, 15.1, and 5.43 J for laser powers of 75.9, 43.5, and 24.1 GW, respectively. In

the simulations, 24.1 GW was sufficient to achieve the objective of a mean gas temperature of 100 eV over the region to be compressed, and the transmitted energy was 23.6 J. Therefore, a power of 75.9 GW with a pulse duration of 1.5 ns, giving a total laser energy of 114 J and a transmitted energy of 36.1 J, should exceed 100 eV but fall short of 200 eV, which was achieved in the simulations with ~ 100 J of transmitted energy at 75.9 GW.

The transmitted intensities as a function of time at all three angles for shot 76679 are shown in Fig. 154.43; the results for the other two shots differ only significantly in their timing, as seen in the direct transmission. Intensity is used here so that the smaller H17C can be compared to 25 and 30. Sidescatter is measured only for a brief period during the transition to total transmission. The simulations roughly match the timing and duration of the sidescatter, but at a much lower level. Sidescatter of transmitted light occurs in the simulations because of refraction around the lip of the remaining overdense foil plasma, seen in Fig. 154.42 from 0.45 ns onward, and because of focusing by the electron density profile of the underdense foil plasma. A better illustration of these features in the simulations is given by Fig. 154.44, which gives the deposited power density with electron density contours overlaid for shot 76676 at 0.7 ns, the time of the peak in sidescattered transmission. The measurements imply either that the hole in the foil is much smaller and the focusing of the transmitted beam is much greater than seen



E27095JR
Figure 154.43
Transmitted laser intensities at ports 25, H17C, and 30 as a fraction of the mean laser intensity at the laser port versus time for shot 76679 (foil, 190 J), with the simulated results, and the incoming laser intensity.



E27096JR
Figure 154.44
Deposited power density, normalized to a maximum value of 1, and electron density contours from the simulation for shot 76676 (foil, 186 J) at 0.7 ns, when sidescattered transmission peaks.

in the simulations, or that just the focusing in the underdense plasma is much greater.

The reflected intensities at all three angles for shot 76676 (186 J) are shown in Fig. 154.45; they are shown again in Fig. 154.46 combined with the transmitted intensities for shot 76679 (190 J). The reflected intensities measured for shot 76677 (103 J), as a fraction of the laser intensity, are practically identical. Reflection is measured only prior to the rapid increase in transmission. Initially, only direct (specular) reflection is measured, with the sidescattered signals rising later on; in other words, the reflected light is spread over an increasing angle until it ceases. The falling edges of all three signals match quite closely and coincide with the initial fall in direct transmission. The magnitude of the simulated reflections differs by so much that they are difficult to fit on the same graph as the measurements; the simulated signal in 25 is much higher and lasts throughout the laser pulse, which is not surprising given that the simulations never show total transmission, and the H17C and 30 signals have been multiplied by a factor of 100 to be visible. The simulations also show a higher reflectivity for the lower energy shot 76679, whereas the measurements show no change in percentage reflectivity. The simulated timings for all three signals do match the measurements reasonably well, considering just the initial rise for 25. The sidescattered

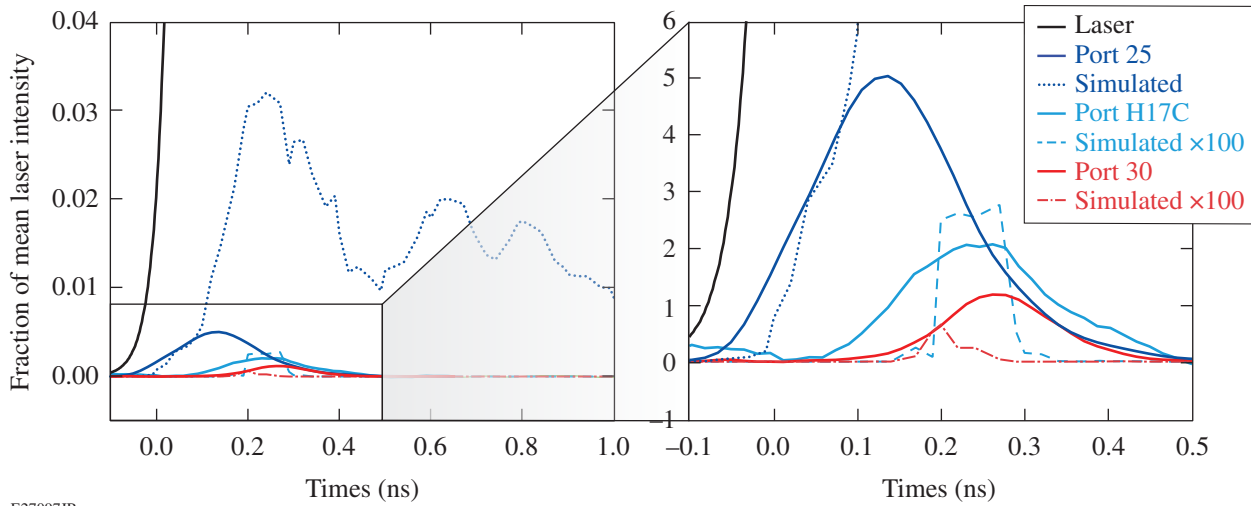


Figure 154.45 Reflected laser intensities at ports 25, H17C, and 30 as a fraction of the mean laser intensity at the laser port versus time for shot 76676 (foil, 186 J) with the simulated results and the incoming laser intensity.

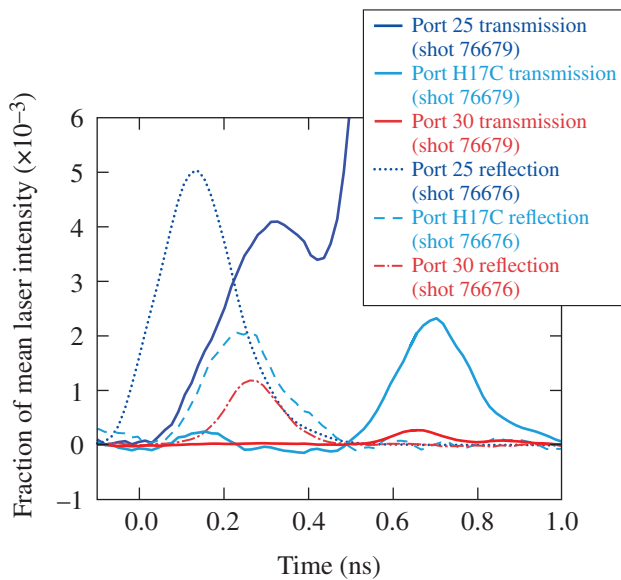


Figure 154.46 Transmitted laser intensities from shot 76679 (foil, 190 J) and reflected laser intensities from shot 76676 (foil, 186 J) as fractions of the mean laser intensity at the laser port versus time.

reflection occurs in the simulations because of curvature of the overdense plasma, seen in Fig. 154.42 at 0.3 ns. It is possible that the simulations underestimate this curvature. However, since reflection occurs before the foil becomes underdense, the simulations could also be in error because they have no accurate physical model for solids and overdense plasma.

Overall, this initial phase of reflection, and transmission, is not energetically significant.

Streaked spectra of the transmitted light measured for shot 76679 in ports 25 and H17C are given in Fig. 154.47; port 30 looks similar to H17C, and the spectra from the other shots differ principally in timing. There is a lot of structure in the direct transmitted spectrum, which is a result of SSD. The simulations do not include SSD, using a delta function wavelength distribution at 351 nm, so they are not directly comparable. There is a red shift in all of the transmitted light signals during the transition to total transmission, which is the only time signal seen in H17C and 30.

All of the spectra for shot 76679—integrated over 0.6 to 0.8 ns, the duration of the emission in H17C and 30—are shown in Fig. 154.48. The red shift is seen to increase with angle, from 25 to H17C to 30. The simulated results are significantly narrower because they do not include the initial bandwidth and the instrument broadening, but they clearly show a smaller blue shift that is larger in 25 than in H17C and 30, the complete opposite of the measurements. The blue shift is caused by the axial velocity of the plasma expanding behind the foil. The red shift seen in the measurements could be caused by a rapid drop in plasma density or by plasma motion away from the detector, at a speed much greater than those achieved in the simulations. There is certainly a rapid drop in plasma density between 0.6 and 0.8 ns because the transmitted powers show that there is practically nothing in the path of the laser shortly

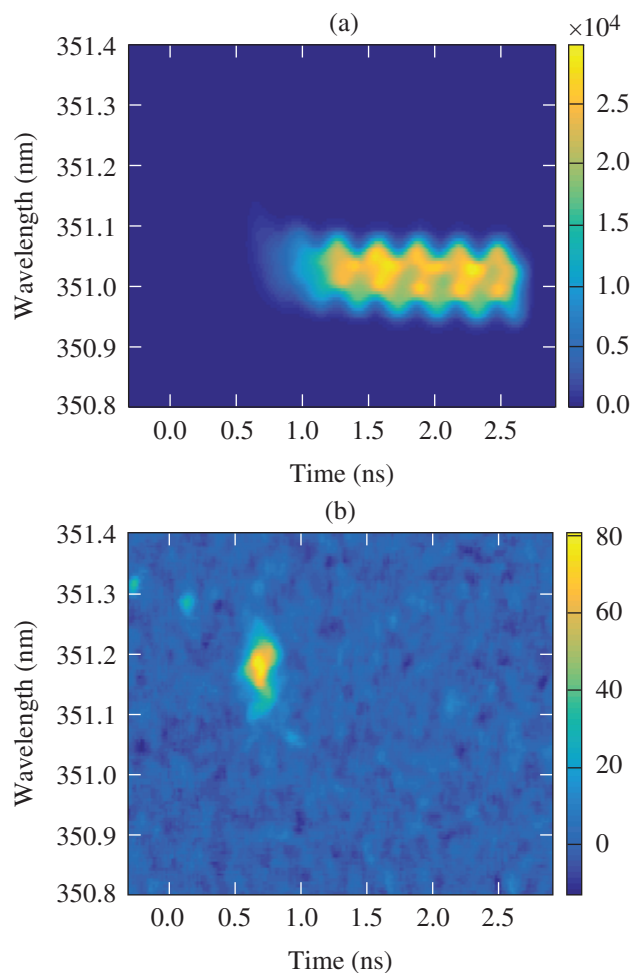
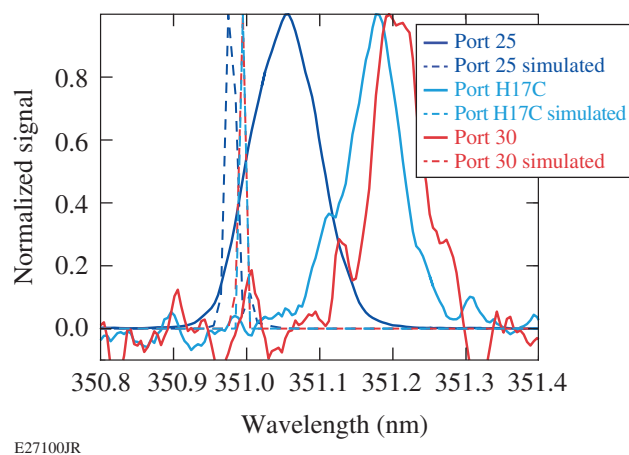


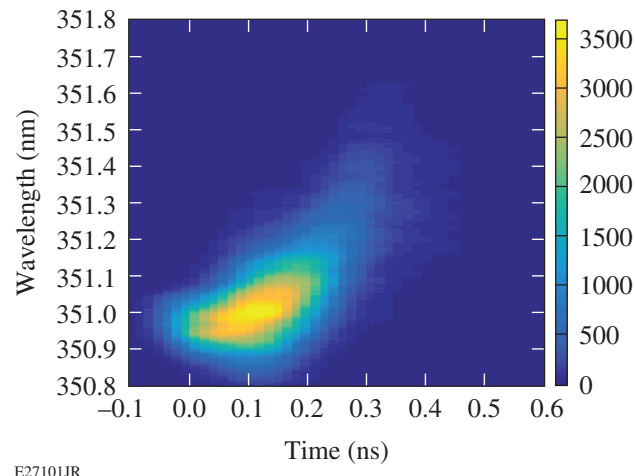
Figure 154.47
Transmission data from the streaked spectrometers in (a) 25 and (b) H17C for shot 76679 (foil, 190 J). A mean background level has been subtracted.

after 0.8 ns. The axial plasma expansion cannot be significantly faster than in the simulations because that would require higher absorption. The only way to achieve rapid evacuation of the plasma from the beam path is radial motion. If the plasma is being pushed out rapidly in the radial direction, the red shift could also be caused by reflection from the radially expanding plasma, which would give a greater shift at larger angles, as observed.

The streaked spectrum of reflected light measured for shot 76676 in port 25 is given in Fig. 154.49; H17C and 30 show similar signals, but they are too close to the background level to readily distinguish features; the results for shot 76677 look very similar. The initial blue shift, seen up to ~0.2 ns, can be caused by plasma expansion from the foil surface and by ionization of the foil. The red shift, which increases throughout the duration



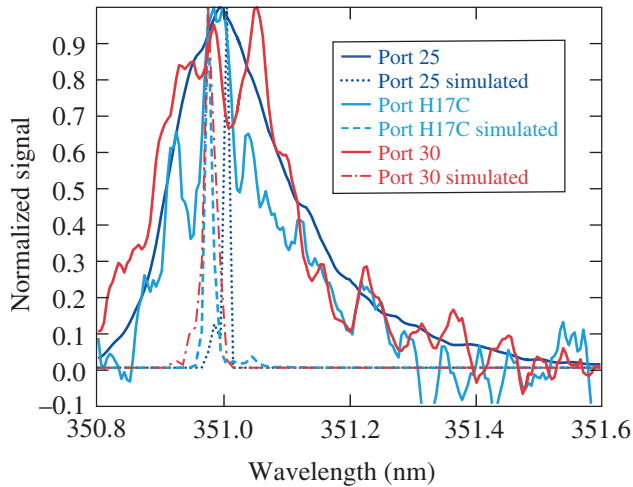
E27100JR
Figure 154.48
Spectra of transmitted light for shot 76679 (foil, 190 J) integrated over the duration of the measured, sidescattered signals, normalized to a peak value of 1, with the results from the simulation for shot 76676 (foil, 186 J).



E27101JR
Figure 154.49
Reflection data from the streaked spectrometer in 25 for shot 76676 (foil, 186 J). A mean background level has been subtracted.

of the signal, is almost certainly caused by the overdense portion of the foil being accelerated in the direction of the laser beam, which can be seen in the simulations in Fig. 154.42.

All of the spectra for shot 76676 integrated over 0 to 0.5 ns, the duration of the measured signal, are shown in Fig. 154.50. It is difficult to compare the measured and simulated values because the simulations do not include the initial bandwidth and instrument broadening, and the measured values for H17C and 30 have a low signal-to-noise ratio. The simulation does show a combination of blue and red shifts, with the exception of 30, which shows only a blue shift, but the magnitude of the red shift



E27102JR

Figure 154.50
Spectra of reflected light for shot 76676 (foil, 186 J) integrated over the duration of the measured signals, normalized to a peak value of 1, with the results from the simulation.

is clearly lower than measured, indicating that the simulations underestimate the inward acceleration of the overdense plasma.

2. Full Targets

The energies collected in the SBS (laser) channel of the time-resolved spectrometers in ports 25, H17C, and 30 are

given in Table 154.V, with the simulated values underneath. The values from the two foil shots that measured reflection are included for ease of comparison.

The most significant results from Table 154.V for the laser-driven MagLIF project show that reflection from full targets is small and comparable to the foil shots, indicating that the transmission of the foils in the full targets should also be comparable to the transmission measured for foils alone. There is no sign of SBS, or SRS, from the gas. Therefore, we expect the simulations to be adequate for the gas heating, giving a slight underestimate because of the underestimate of the energy transmitted by the foil.

The mean direct reflectivity for the two foils is $0.048 \pm 0.004\%$ (standard error plus uncertainty from the calibration) and for the five full targets is $0.038 \pm 0.014\%$, so they can be considered to be in agreement within the uncertainties. The simulations give 1.6% for the nominally 200-J shots on foils and full target and 2.3% for the nominally 100-J shot on a foil; the measurements do not indicate a variation in reflectivity over this energy range, but there is only one shot at 100 J. Using a Gaussian to extrapolate the energy outside port 25 from the energy per area measured in H17C and 30 gives total reflectivities of $0.61 \pm 0.10\%$ and $0.59 \pm 0.22\%$ for foils and full targets, respectively, which are in good agreement. The total reflectivity in the simulations

Table 154.V: Results for full targets, giving fill pressure (*P*), laser energy (*E*), and reflected laser energy collected by the diagnostics in ports 25 (the laser port), H17C, and 30, with simulated results underneath, and the reflection measurements made with foils for ease of comparison. The percentage in parentheses is with respect to the energy per unit area at the laser port. The calibration errors are estimated at $\pm 7\%$ for 25, $\pm 16\%$ for H17C, and $\pm 14\%$ for 30, as explained in the text.

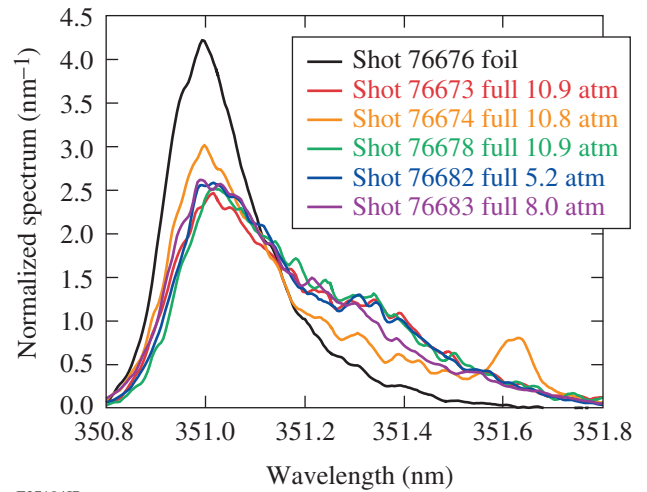
<i>P</i> (atm)	<i>E</i> (J)	25 (%) Simulation	H17C (%) Simulation	30 (%) Simulation
10.9	193	65.1 mJ (0.034)	0.159 mJ (0.015)	19.7 mJ (0.01)
		3.12 J (1.6)	1.03 μ J (<0.001)	25.7 μ J (<0.001)
10.8	192	53.1 mJ (0.028)	0.172 mJ (0.016)	21.2 mJ (0.011)
		3.10 J (1.6)	1.02 μ J (<0.001)	25.5 μ J (<0.001)
10.9	182	45.9 mJ (0.025)	96.9 mJ (0.010)	9.18 mJ (0.005)
		3.03 J (1.7)	1.14 μ J (<0.001)	44.5 μ J (<0.001)
5.2	199	118 mJ (0.059)	0.177 mJ (0.016)	14.6 mJ (0.007)
		3.21 J (1.6)	1.05 μ J (<0.001)	26.4 μ J (<0.001)
8.0	191	118 mJ (0.062)	0.108 mJ (0.010)	10.6 mJ (0.016)
		3.09 J (1.6)	1.02 μ J (<0.001)	25.5 μ J (<0.001)
Foil	186	85.0 mJ (0.046)	0.161 mJ (0.016)	14.6 mJ (0.008)
		3.23 J (1.7)	0.946 μ J (<0.001)	27.3 μ J (<0.001)
Foil	103	51.0 mJ (0.050)	0.101 mJ (0.016)	8.63 mJ (0.008)
		2.35 J (2.3)	35.1 nJ (<0.001)	1.55 μ J (<0.001)

is practically the same as the direct reflectivity, given above, because the simulations have negligible sidescatter.

The reflected intensities as a function of time measured in ports 25 and 30 are given in Fig. 154.51. The results for H17C give a similar picture to 30 but with a higher noise level. The direct reflection in all of the full target shots rises later and more sharply than for the foils and in some shots shows a slower decay. The sidescattered reflections from full targets vary in timing and last slightly longer than the sidescattered reflections from foils. These observations are consistent with the foils on the full targets curving outward, as seen in Fig. 154.38, which would lead to an initial specular reflection being spread over a greater angle and to the overdense foil initially flattening out as it is driven inward. Curvature could also explain why the direct reflected energy varied significantly but not the total reflected energy, as inferred from the Gaussian extrapolation. The variations seen in the full targets could be because of variations in the curvature, in the position of the beam relative to the center of the foil (positioning accuracy is at best $\pm 10 \mu\text{m}$), and in the angle of the target. Fixing the cylinders at the correct angle to the target mount was found to be an issue with the early targets, and the angle varied by $\pm 2^\circ$; since the OMEGA Target Positioning System has no tip-tilt adjustment, we could not compensate for this issue. The angles are now carefully measured and all targets fielded are off by less than 1° .

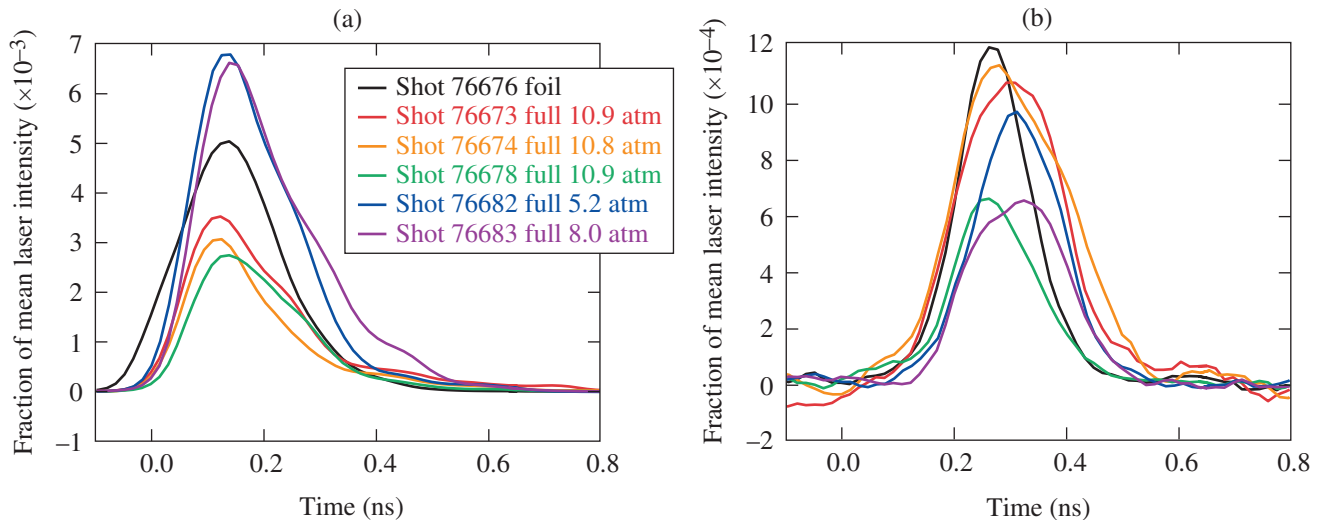
The direct reflected spectra are given in Fig. 154.52; the sidescattered spectra are too noisy to distinguish any details.

The full targets all show a greater red shift than the foils alone, indicating a greater inward acceleration. The greater acceleration of the foils on full targets could be caused by the thinning caused by the gas pressure exceeding their elastic limit, resulting in less mass to be accelerated. It is also possible that the walls of the cylinder lead to a slower radial expulsion of the foil plasma, which appears to be the only explanation for the rapid transition to total transmission seen with the foils alone. With the foil



E27104JR

Figure 154.52 Direct reflected spectra, normalized so that the area under the curve is 1, for all shots except shot 76677 (foil, 103 J), which is very similar to that for shot 76676.

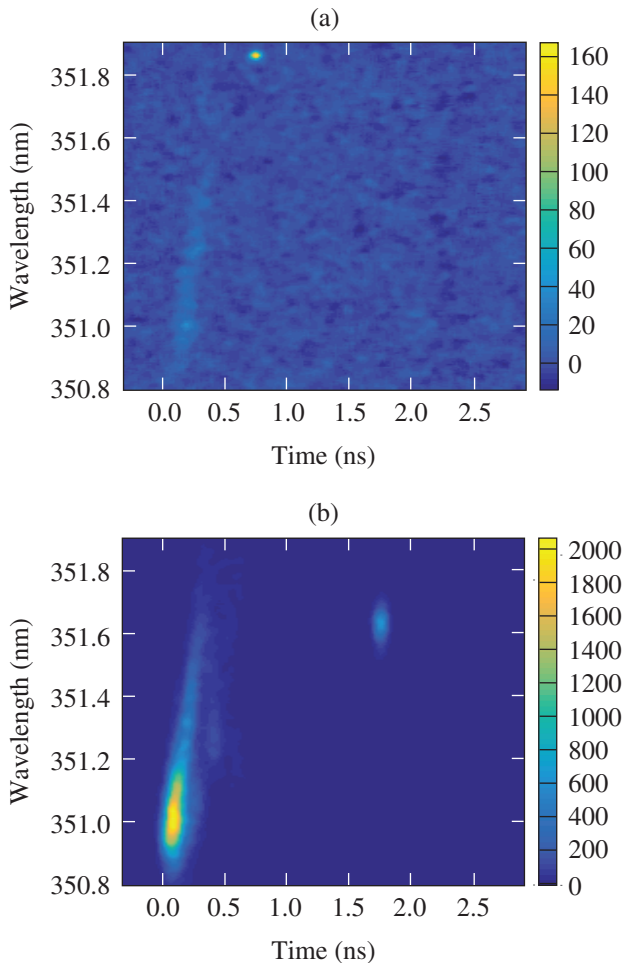


E27103JR

Figure 154.51 Reflected intensities in (a) 25 and (b) 30 for all shots except shot 76677 (foil, 103 J), which is very similar to that for shot 76676.

plasma remaining longer in the path of the beam, reflection will last longer and the overdense plasma could be accelerated for a longer time, which is consistent with the observations.

One unique feature was seen in the reflections from two of the full targets (shots 76673 and 76674): a brief red-shifted reflection at some time after the main signal and at different angles in each shot, shown in Fig. 154.53. This feature is responsible for the peak near 351.6 nm seen in Fig. 154.52 for shot 76674, but it cannot be seen in the reflected intensity given in Fig. 154.51 because the time axis does not extend far enough. It is possible that a similar signal coinciding with the main signal is present in other shots, contributing to the variation in the signals. We believe that this is a reflection from the back of the target, which would be determined by the bend in



E27105JR

Figure 154.53
Reflection data from streaked spectrometers for shots (a) 76673 (full, 193 J) and (b) 76674 (full, 192 J) that show an additional signal at later times and longer wavelengths, not seen in other shots.

the fill tube, as seen in Fig. 154.38(c), which varied from shot to shot. It is also possible that the glue used to fix the cylinder and the fill tube into the target mount partially occluded the hole, causing a reflection.

Conclusions

We have demonstrated that (1) the transmission of the 1.84- μm -thick polyimide foils selected for the preheat laser entrance windows of OMEGA MagLIF targets is sufficient for the gas to heat to >100 eV, (2) sidescatter of the transmitted light is at an acceptable level, and (3) there is no measurable SBS or SRS backscatter from the gas.

Based on the foil transmission measurements and simulations of the gas heating, for the 1.5-ns square-shaped pulses used in current OMEGA MagLIF experiments, a preheat laser energy of 100 J should be sufficient to preheat the gas to a mean temperature of 100 eV. Currently, experiments use 180 J, which according to simulations⁶ is the highest energy that will not lead to significant wall blow-in before compression, and achieve a mean temperature of about 200 eV, the preheat temperature initially chosen for the point design.⁶

Simulations of the experiments using a 2-D radiation–hydrodynamic code with 3-D ray tracing and inverse bremsstrahlung energy deposition underestimated direct laser transmission, by $\sim 10\%$ of the laser energy, because the underdense foil plasma continued to absorb laser energy throughout the pulse, whereas the measurements show a rapid transition to total transmission. The simulations also significantly overestimated the direct reflection because this also continued throughout the pulse, significantly underestimated sidescattering of transmitted and reflected light, and significantly underestimated the red shift of transmitted and reflected light.

We believe that the disagreement between the measurements and simulations is caused by relativistic self-focusing of the laser, enhanced by self-focusing resulting from the electron density profile, followed by ponderomotive blowout of the foil plasma. The simulations do not include relativistic self-focusing or the ponderomotive force.

The minimum laser power required for relativistic self-focusing is¹¹

$$P = 16.6 \frac{n_c}{n_e} \text{ GW}; \quad (4)$$

therefore, the lowest laser power used can self-focus at an electron density of $0.69 n_c \leq n_e < n_c$, and the highest laser power at

$0.21 n_c \leq n_e < n_c$. The simulations show that the electron density profile formed also acts to focus the laser, so the two mechanisms could enhance one another. The ponderomotive potential will become significant if it exceeds the electron temperature. The highest electron temperature reached in the simulations was ~ 1 keV, which is exceeded by the ponderomotive potential¹² at the lowest laser power used if it is focused to $R < 3.0 \mu\text{m}$ (8.5λ); at the highest laser power, this increases to $5.5 \mu\text{m}$ (16λ). The minimum value of R for which the theory of Gaussian beams is valid is $\lambda/\sqrt{2}\pi$, which would give a ponderomotive potential in excess of 1 MeV. It is interesting to note that a beam with sufficient power for relativistic self-focusing does have a relativistic intensity ($I\lambda^2 > 10^{18} \text{ W/cm}^2 \mu\text{m}^2$ or 10 GW) when focused to a spot width $\sim \lambda$, and its ponderomotive force is then sufficient to separate the electrons from the ions.¹³ Expulsion of electrons by the ponderomotive force provides an additional mechanism for self-focusing, prior to the expulsion of the ions, so we potentially have three synergistic focusing mechanisms. Therefore, self-focusing can occur and can lead to the ponderomotive force of the focused laser expelling the plasma radially.

Self-focusing followed by ponderomotive blowout provides a qualitative explanation for all of the observations not accounted for by the simulations. The rapid transition to total transmission can be explained by the ponderomotive force of the focused beam expelling the plasma radially until the beam path is clear. The observation of total transmission indicates that there is practically no plasma in the path of the beam, and the only way to achieve this is radial expulsion of the plasma because an expansion similar to that observed in the simulations, but at a significantly higher velocity, would require a higher absorption. The higher sidescattered transmission, seen during the transition to total transmission, can be explained by the small focal spot achieved prior to the blowout of the plasma; the circular diffraction extrapolation applied to the energy per area collected in H17C and 30 implied a time-averaged source radius of 0.8 to 1.27λ for laser energies of 60 to 190 J, which is consistent with the degree of focusing required to achieve ponderomotive blowout. The higher red shift of the transmitted light, which increased with angle, can be explained by the rapid drop in plasma density and reflection from the edges of the expanding plasma channel formed. The higher sidescattered reflection and the greater red shift of the reflected light could be explained by initial self-focusing in the blowoff plasma, before the foil becomes underdense, leading to greater curvature and acceleration of the overdense foil.

Another implication of this mechanism is that the propagation of foil into the gas will not be accurately simulated; radial

expulsion of the foil should reduce the quantity of foil pushed into the gas, but the increase in laser intensity could push any remaining foil material farther inward.

Relativistic self-focusing and ponderomotive blowout can lead to the formation of N separate filaments if the laser power exceeds NP , and the spot size is large enough.¹³ Given that the lowest power used appears to be capable of reaching this regime, the highest power should be able to produce three filaments. Our diagnostics cannot determine whether or not this occurred. In any case, the eventual expulsion of the plasma leads to this being only a brief phase, as seen in the transmission measurements.

The gas density used in these experiments ($0.067 n_c$) is too low for relativistic self-focusing to occur, even at the highest laser power used. Therefore, once the laser has expelled the foil plasma, laser propagation and heating should be adequately described by the simulations, which are currently our best means of determining the gas temperature.

Experiments with a laser power less than 16 GW would provide a means of verifying that relativistic self-focusing is the mechanism responsible for the observations, but this power is too low for laser preheating in MagLIF, so it was not considered.

Currently, we do not have the capability to simulate the effect of relativistic self-focusing and the ponderomotive force in these experiments. Including the ponderomotive force in a hydrocode would lead to a complex interaction between the ray tracing and the hydrodynamics, and the code would have technical problems with holes appearing in the fluid. Furthermore, the ponderomotive force can lead to significant charge separation,¹³ which would require at least a two-fluid model to be dealt with adequately. Three-dimensional PIC (particle-in-cell) code simulations, which would capture relativistic self-focusing, the ponderomotive force, and charge separation in a fully self-consistent manner, are not practical for the time and space scales of interest, particularly if collisions are to be included.

Z experiments use higher laser powers than used here, typically 0.5 TW, so relativistic self-focusing and ponderomotive blowout could also be occurring. However, the power and duration of the prepulse used can be too low for relativistic self-focusing and ponderomotive blowout to occur, and the prepulse lowers the plasma density seen by the main pulse. On the other hand, the higher power and longer wavelength (527 nm)

of the Z Beamlet laser means that relativistic self-focusing of the main pulse could occur in the gas. The typical deuterium density used in Z experiments⁴ is 0.7 mg/cm^3 , giving a power threshold of 0.28 TW at 527 nm.

At a wavelength of 351 nm and with pulse shaping available for the preheating beam, it would be possible to avoid relativistic self-focusing in MagLIF preheating, at all scales, if this turns out to be desirable. For the OMEGA MagLIF experiments, where the pulse shape of the preheating beam must be the same as the compression beams, it would appear to be beneficial because it increases transmission and potentially reduces the amount of foil material driven into the target. On the other hand, there is an advantage in remaining in a regime where our simulation tools are known to be valid in order to have a predictive capability.

ACKNOWLEDGMENT

The information, data, or work presented herein was funded in part by the Advanced Research Projects Agency-Energy (ARPA-E), U.S. Department of Energy, under Award Number DE-AR0000568, the Department of Energy National Nuclear Security Administration under Award Number DE-NA0001944, the University of Rochester, and the New York State Research and Development Authority. The support of the DOE does not constitute an endorsement by the DOE of the views expressed in this paper.

REFERENCES

1. S. A. Slutz, M. C. Herrmann, R. A. Vesey, A. B. Sefkow, D. B. Sinars, D. C. Rovang, K. J. Peterson, and M. E. Cuneo, *Phys. Plasmas* **17**, 056303 (2010).
2. A. B. Sefkow, S. A. Slutz, J. M. Koning, M. M. Marinak, K. J. Peterson, D. B. Sinars, and R. A. Vesey, *Phys. Plasmas* **21**, 072711 (2014).
3. M. M. Basko, A. J. Kemp, and J. Meyer-ter-Vehn, *Nucl. Fusion* **40**, 59 (2000).
4. M. R. Gomez, S. A. Slutz, A. B. Sefkow, D. B. Sinars, K. D. Hahn, S. B. Hansen, E. C. Harding, P. F. Knapp, P. F. Schmit, C. A. Jennings, T. J. Awe, M. Geissel, D. C. Rovang, G. A. Chandler, G. W. Cooper, M. E. Cuneo, A. J. Harvey-Thompson, M. C. Herrmann, M. H. Hess, O. Johns, D. C. Lamppa, M. R. Martin, R. D. McBride, K. J. Peterson, J. L. Porter, G. K. Robertson, G. A. Rochau, C. L. Ruiz, M. E. Savage, I. C. Smith, W. A. Stygar, and R. A. Vesey, *Phys. Rev. Lett.* **113**, 155003 (2014); P. F. Schmit, P. F. Knapp, S. B. Hansen, M. R. Gomez, K. D. Hahn, D. B. Sinars, K. J. Peterson, S. A. Slutz, A. B. Sefkow, T. J. Awe, E. Harding, C. A. Jennings, G. A. Chandler, G. W. Cooper, M. E. Cuneo, M. Geissel, A. J. Harvey-Thompson, M. C. Herrmann, M. H. Hess, O. Johns, D. C. Lamppa, M. R. Martin, R. D. McBride, J. L. Porter, G. K. Robertson, G. A. Rochau, D. C. Rovang, C. L. Ruiz, M. E. Savage, I. C. Smith, W. A. Stygar, and R. A. Vesey, *Phys. Rev. Lett.* **113**, 155004 (2014).
5. D. H. Barnak, J. R. Davies, R. Betti, M. J. Bonino, E. M. Campbell, V. Yu. Glebov, D. R. Harding, J. P. Knauer, S. P. Regan, A. B. Sefkow, A. J. Harvey-Thompson, K. J. Peterson, D. B. Sinars, S. A. Slutz, M. R. Weis, and P.-Y. Chang, *Phys. Plasmas* **24**, 056310 (2017).
6. J. R. Davies, D. H. Barnak, R. Betti, E. M. Campbell, P.-Y. Chang, A. B. Sefkow, K. J. Peterson, D. B. Sinars, and M. R. Weis, *Phys. Plasmas* **24**, 062701 (2017).
7. E. C. Hansen, D. H. Barnak, R. Betti, E. M. Campbell, P.-Y. Chang, J. R. Davies, V. Yu. Glebov, J. P. Knauer, J. Peebles, S. P. Regan, and A. B. Sefkow, *Plasma Phys. Control. Fusion* **60**, 054014 (2018).
8. S. P. Regan, R. Epstein, B. A. Hammel, L. J. Suter, J. Ralph, H. Scott, M. A. Barrios, D. K. Bradley, D. A. Callahan, C. Cerjan, G. W. Collins, S. N. Dixit, T. Doeppner, M. J. Edwards, D. R. Farley, S. Glenn, S. H. Glenzer, I. E. Golovkin, S. W. Haan, A. Hamza, D. G. Hicks, N. Izumi, J. D. Kilkenny, J. L. Kline, G. A. Kyrala, O. L. Landen, T. Ma, J. J. MacFarlane, R. C. Mancini, R. L. McCrory, N. B. Meezan, D. D. Meyerhofer, A. Nikroo, K. J. Peterson, T. C. Sangster, P. Springer, and R. P. J. Town, *Phys. Plasmas* **19**, 056307 (2012).
9. M. Geissel *et al.*, *Phys. Plasmas* **25**, 022706 (2018).
10. A. J. Harvey-Thompson, A. B. Sefkow, T. N. Nagayama, M. S. Wei, E. M. Campbell, G. Fiksel, P.-Y. Chang, J. R. Davies, D. H. Barnak, V. Y. Glebov, P. Fitzsimmons, J. Fooks, and B. E. Blue, *Phys. Plasmas* **22**, 122708 (2015); A. J. Harvey-Thompson, A. B. Sefkow, M. S. Wei, T. Nagayama, E. M. Campbell, B. E. Blue, R. F. Heeter, J. M. Koning, K. J. Peterson, and A. Schmitt, *Phys. Rev. E* **94**, 051201 (2016).
11. P. L. Kelley, *Phys. Rev. Lett.* **15**, 1005 (1965); **16**, 384(E) (1966).
12. P. Mora and T. M. Antonsen, Jr., *Phys. Rev. E* **53**, R2068 (1996); P. Mora and T. M. Antonsen, Jr., *Phys. Plasmas* **4**, 217 (1997).
13. F. Cattani *et al.*, *Phys. Rev. E* **64**, 016412 (2001); A. Kim *et al.*, *Phys. Rev. E* **65**, 036416 (2002).